JAAS

Journal of Analytical Atomic Spectrometry

Accepted Manuscript

This article can be cited before page numbers have been issued, to do this please use: H. J. Whitlow, G. Nagy, R. J. W. Frost, D. Toyen, D. Bose, A. McLaughlin, K. M. Smith, C. G. Ryan, A. Azarov, A. Kuznetsov and F. Villinger, *J. Anal. At. Spectrom.*, 2026, DOI: 10.1039/D5JA00505A.

View Article Online
DOI: 10.1039/D5JA00505A

Journal Name

ARTICLE TYPE

Cite this: DOI: 00.0000/xxxxxxxxxx

Ion microprobe determination of ex vivo trace element molarities: The LINAEUS code suite†

Harry J. Whitlow,*[a,b,††] Gyula Nagy,[c,d‡] Robert J. W.Frost,[c] Donruedee Toyen,[c,e] Deepanwita Bose[f,g¶], Aaron McLaughlin,[g] Karen M. Smith,[h] Chris G. Ryan,[i] Alexander Azarov,[b] Andrej Kuznetsov,[b] and Francois Villinger[f,g,h]

Received Date
Accepted Date

DOI: 00.0000/xxxxxxxxxx

MeV-ion based analytical methods such as Particle induced X-ray Emission (PIXE) using a MeV ion microprobe in conjunction with analysis codes such as GeoPIXE represent powerful methods for analysis of trace elements in biomedical samples. In order to make the method truly quantitative for thin biological samples, knowledge of the local composition and thickness is required. Here the development and application of the LINAEUS code package, a complementary companion code to GeoPIXE code is described. This provides regional major element (C, H, N and O) composition and thickness data from Elastic Backscattering Spectrometry (EBS) and Off-Axis Scanning Transmission Ion Microscopy (OA-STIM) measurements. The program suite employs the same Dynamic Analysis method as used in GeoPIXE. LINAEUS incorporates a tissue region detection procedure based on spatial correlation to mitigate bias due to void regions without tissue corresponding to blood vessels etc. The results for healthy murine small-intestine tissue showed no differences in the C, H, N and O contents but did show differences in thickness that were attributed to morphological distortion during drying of the tissue section. The molarity of trace elements (S, Cl, K, Ca and Fe) exhibited differences between tissue regions. Ca "hot-spots" (10-30 μm regions with much enhanced Ca levels) reported in other simian tissue samples were observed. These could not be attributed to mineralisation and their origin remains unclear.

1 Introduction

The molar concentration of lesser and trace elements in ex vivo tissue are quantities of physiological importance in trace element biomedicine. Physical analytical methods such as Particle Induced X-ray Emission (PIXE) using a MeV ion microprobe are powerful for quantification and imaging of trace elements in tissue sections [1–3]. A significant drawback of these methods has been that in-vacuum analysis implies the content of lesser/trace content element i is quantified in terms of a mass ratio m_i/m_m to a dry tissue matrix (e.g. μg/g). m_i is the mass of element i and m_m the mass of the dry tissue matrix. The dry tissue matrix being the ex vivo tissue after loss of H_2O on dehydration and is mostly C, H, N and O. Here ex-vivo is taken to refer to wet tissue immediately after removal from the subject. The molarity expresses the concentration of a substance as the ratio of two SI base units, the quantity of a substance in moles per unit volume [4].

Tissue sections are typically made up of regions of different cell types. These regions can have different major element compositions and contain 65 to 90 mass % H_2O, which is lost on analysis leading to different dry matrix C, H, N, O, atomic compositions and thickness [5,6]. A further consideration is that the structure of the different biological tissue-types within a sample can give rise to natural thickness inhomogeneity in the form of void re-

* Corresponding author
[a] Tandem Laboratory, Uppsala University, PO Box 529, SE-751 21 Uppsala, Sweden: E-mail: Harry.whitlow@physics.uu.se
[b] Department of Physics, University of Oslo, Blindern, Oslo, N-0316, Norway
[c] Department of Physics and Astronomy, Uppsala University, PO Box 516, SE-751 20, Uppsala, Sweden.
[d] Institute of Applied Physics, TU Wien, Vienna. 1040, Austria.
[e] Department of Materials Science, Kasetsart University, Faculty of Science, Bangkok, 10900, Thailand.
[f] Michael E. Keeling Center for Comparative Medicine and Research, The University of Texas, MD Anderson Cancer Center, 650 Cool Water Drive, Bastrop, TX 78602, USA.
[g] New Iberia Research Center, University of Louisiana at Lafayette, P.O. Box 13610, New Iberia, LA 70562, USA.
[h] Department of Biology, University of Louisiana at Lafayette, P.O. Box 43602, Lafayette, LA 70504, USA.
[i] CSIRO Mineral Resources, Clayton, VIC 3168, Australia
[††] Present address: Tandem Laboratory, Uppsala University, PO Box 529, SE-751 21 Uppsala, Sweden.
[‡] Present address: Institute of Applied Physics, TU Wien, Vienna. 1040, Austria.
Present address: Department of Materials Science, Kasetsart University, Faculty of Science, Bangkok, 10900, Thailand.
[¶] Present address: Michael E. Keeling Center for Comparative Medicine and Research, MD Anderson Cancer Center, The University of Texas, 650 Cool Water Drive, Bastrop, TX 78602, USA.

† Supplementary Information available:

View Article Online
DOI: 10.1039/D5JA00505A

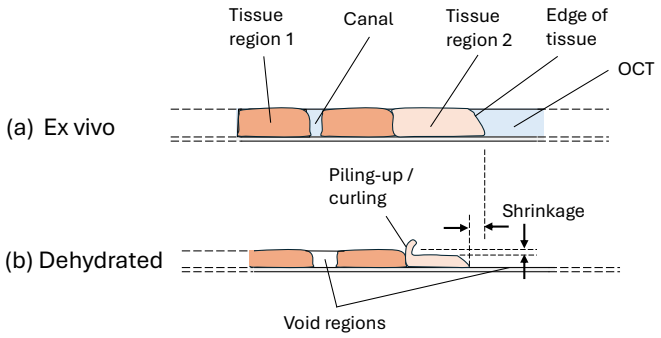

Fig. 1 Dehydration-induced morphological changes of a biological tissue section. (a) Ex vivo tissue section after cryosectioning. (b) Dry tissue section after dehydration.

gions with no tissue present. These are associated with blood vessels, lymph canals, villi etc. Moreover, mechanical distortion on dehydration can result in artefacts such as shrinkage, tears, overlapping, piling-up, curling etc. as illustrated in Figure 1. Biological tissue sections are often intermediate between the PIXE thin and thick target thickness cases[7]. The thickness variations will likely cause significant lesser- and trace-element concentration variations such as those observed in an early study on Simian Immunodeficiency Virus (SIV) infected jejunum tissue[3]. A consequence of such composition and thickness variations is that the yields of lesser and trace-element characteristic X-rays can vary from one tissue region to another for the dry tissue section. To overcome these difficulties a method has been developed that is based on measurement of the C, H, N and O content and region thickness using Elastic Backscattering Spectrometry (EBS) and Off-Axis Scanning Transmission Ion Microscopy (OA-STIM)[5,8–10].

In our previous work PIXE data analysis used the well-established GeoPIXE codes[11–13] while the EBS and OA-STIM analysis was based on a collection of ad-hoc code[9,10]. A difficulty with this approach is that combining EBS, PIXE and OA-STIM with different calibration parameters, kinematic factors and stopping data was tedious and complex.

The goal of this work is to report on development and demonstrate use of the code-suite LINAEUS (LINear Analysis of Elements Using Spectroscopies). This code suite which is driven by a Graphic User Interface (GUI) is tab-structured for ease of use by guiding the user through the different steps. LINAEUS is used to determine the dry tissue matrix element composition and thickness to facilitate the determination of trace element molarities using GeoPIXE. Functionalities are included in LINAEUS to suppress data from void regions as well as handle major element concentration reference data. The goal of this work is to describe the code suite and illustrate its use. To maintain brevity, technical details are given in the supplementary material †.

2 The LINAEUS code suite

The LINAEUS code suite, like GeoPIXE[14,15], is based on the Dynamic Analysis (DA) method. The code-suite uses the EBS and OA-STIM data to produce maps of the major elements (C, H, N and O) as well as major element composition and thickness data for a series of image regions imported from GeoPIXE. This allows the regions for analysis to be selected based on features in the EBS, OA-STIM and PIXE maps. Generally, these elemental images are grainy due to the small number of Poissonian distributed counts in each pixel[16]. LINAEUS makes use of the same Dynamic Analysis approach adopted in GeoPIXE for X-ray spectrum analysis. The Dynamic Analysis procedure determines major element concentrations with reduced stochastic uncertainties from counting statistics by summing the H, C, N and O signals from all pixels in each region. This is done by first performing a non-linear fitting of a prototype function made up of different characteristic lineshapes to an experimental EBS spectrum. This defines the position and shape of the characteristic lineshape for each element. The experimental spectra from different image regions can be represented as a linear combination of the different lineshapes according to their yields. A matrix least-squares linear regression approach[11–13], facilitates each count to be associated with a yield contribution to each elemental lineshape according to its energy. Thus by sequentially reading the energy of each count and its associated (x, y) coordinates from the data file, concentration maps for each element and total content can be accumulated event-by-event. The mathematical formalism where the C, N and O surface concentration of the tissue section is related to the fitted surface-edge heights is provided in the Supplementary material †and described elsewhere[5,9]. The H content cannot be derived from the H signal from OA-STIM in the same way as C, N and O is from the EBS signal. Therefore a pseudo-linearisation is used where the H-concentration is assumed constant over the tissue section thickness. H-surface concentration is then proportional to H_H the mean yield per channel. i.e. $H_H = Y_H/\Delta E$, where Y_H is the total number of H-counts and ΔE is the shift in edge position in channels, which in turn is proportional to the tissue section thickness[8–10].

Since a proton beam is used to analyse H, C, N and O, consideration must be given to the non-Rutherford scattering cross sections[8]. The experimental cross sections[17] on which[18] the SigmaCalc predictor code is based exhibit considerable variations. This would give rise to significant ($\sim$ 5-8 %) uncertainty in the measured major element compositions. Instead, the C, H, N and O calibration uses a thin ($\lesssim 1\mu$m) polymer film. It is convenient to use a blank Pioloform support film for this[19] because the composition is well defined within 1-2 at.%[19]. This also provides an accurate reference value for subtraction of the H background from the support film. Since Piolofiorm does not contain N, the calibration of the N-content is based on the ratio of the N and O scattering cross sections from SigmaCalc[17].

The morphology of 2D biomedical tissue sections often naturally includes void regions such as those associated with blood vessels, lymph canals, villi and crypts. In these void areas there is no tissue covering the support film. This can give rise to a systematic error in the major element composition (and also the thickness) because the EBS signal measures the surface composition of C, N and O in the sample. Void regions in the analysed region then contribute a surface composition component corresponding to the support film.

View Article Online
DOI: 10.1039/D5JA00505A

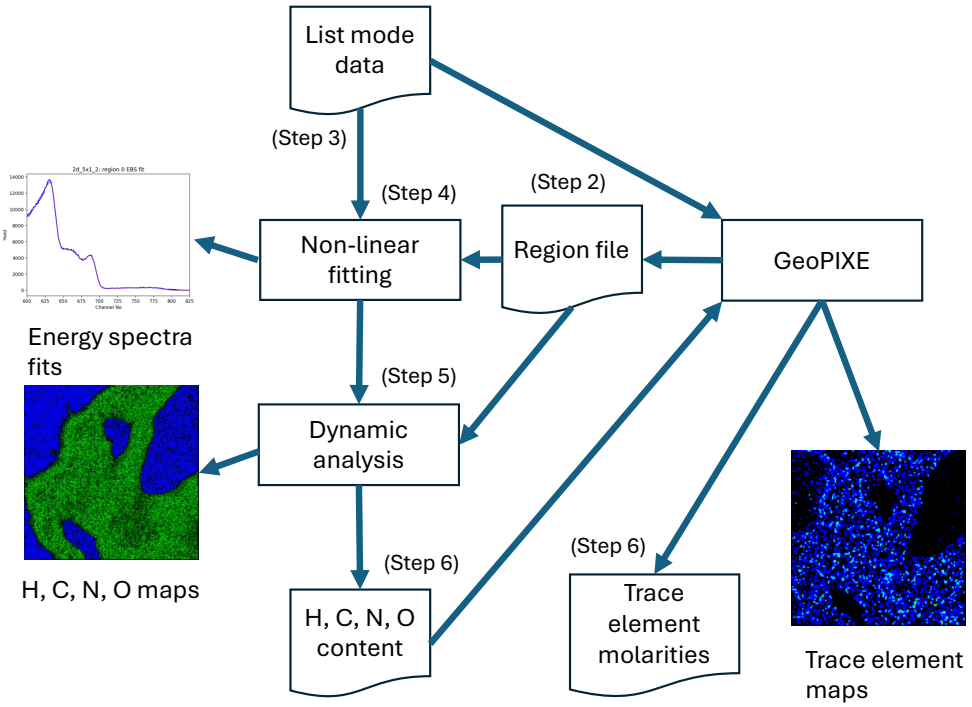

Fig. 2 Schematic illustration of the data analysis procedure with LINAEUS and GeoPIXE. The step number in parentheses refer to the steps in the main text. (Step 1 has been omitted as it can be performed within GeoPIXE or LINAEUS.)

An objective void-region suppression algorithm based on spatial frequencies associated with granularity has implemented to segment the image into void and tissue-covered regions[20]. LINAEUS allows selection of all pixels, or only pixels in the tissue-covered segment to contribute to the composition for each image region.

Communications between the different sub-programs that make-up LINAEUS is by means of human readable and editable .csv format files. The parameters in the configuration files can be edited manually using a spreadsheet program, using the configuration windows in LINAEUS or graphically from the measurement data using the Data Visualizer. The data structure which is described in detail in the Supplementary material †is organised to exploit the communality between samples e.g. one set of calibration data can be used for a large number of samples in the same measurement session. Image data is output as grey-scale images in the loss-less .png format. In numerical analysis of binned data aliasing errors are a common problem. To prevent aliasing errors propagating, the original data is maintained in terms of counts and channel numbers and energy calibrations are only applied when necessary inside each procedure.

The Data Visualizer function in LINAEUS facilitates display of raw EBS, OA-STIM and PIXE energy spectra and yield image maps. This can be used to define regions of maps for analysis as well as setting up energy calibrations and reference sample yields etc.

The GUI is organised as tabs that successively guide the user through the different analysis steps described below in Section 2.1.

2.1 Analysis procedure

As noted above, the analysis procedure using LINAEUS is performed in a series of steps. These are illustrated in Figure 2.

1. *Establishing calibration parameters.* In this stage, the experimental configuration and the calibration parameters are set up. These include the energy calibrations, (A,B where E[keV] $= AE_{ch} + B$) for the PIXE, EBS and OA-STIM spectra. The reference material calibration is also entered at this stage. This includes the yields under the C and O peaks in the EBS spectrum and the H peak in the OA-STIM from the calibration film. These can be determined by sorting the list files using the GeoPIXE code or selected using the spectrum display function used for non-linear fitting. The C, H and O composition of the reference film and a prototype value of the dry tissue matrix composition and density are also defined at this stage. In addition, the files containing 6th order polynomial fits to the stopping and scattering cross section data need to be assigned.

2. *Selection of tissue regions for analysis.* This step is conveniently carried out using GeoPIXE to define the image regions since this allows delineation of the regions based on the EBS, PIXE and OA-STIM X-ray elemental image data. The region definition .csv files from GeoPIXE are subsequently used as input in LINAEUS to define the shapes of the regions.

3. *Conversion of list-mode data to a text event mode file.* The data file organisation used in different microprobe facilities varies

View Article Online
DOI: 10.1039/D5JA00505A

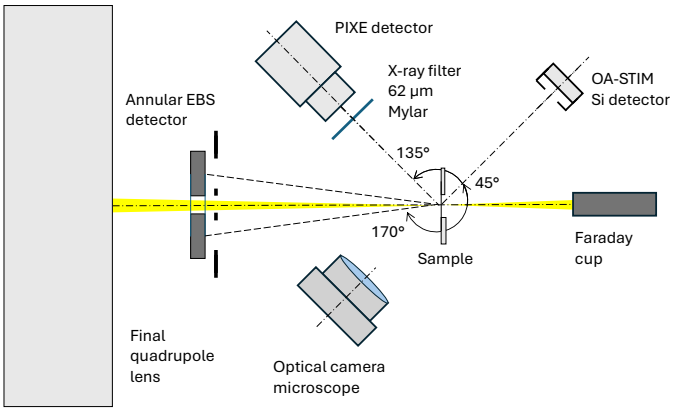

Fig. 3 Schematic illustration of the EBS, OA-STIM and PIXE measurement configuration.

widely. Typically, multi-dimensional histograms, event mode and time stamped-data forms are used. LINAEUS accepts data in a single format (.evt) which is a human-readable text file, arranged in ntuple format where each row corresponds to one detector pulse and contains ADC number, ADC conversion value, (x, y), scan coordinates and (optionally) a time-stamp. (The OMDAQ LmfExtract code outputs a file that is functionally similar to .evt and can be used directly after changing the extension.) Provision is made to easily implement calling external programs which perform the conversion of data files from other microbeam systems.

4. *Non-linear fitting of the prototype EBS spectrum.* In this step the shape and position of the contributions from C, N and O to the EBS spectra are determined. A standard non-linear least-squares regression code is used, where the individual parameters (edge position and width, slope) can be treated as fixed- or free-parameters. Details are given in the Supplementary material †. By fixing and freeing different parameters and fitting over different regions in the EBS spectrum, convergence to sub-optimal local minima could be avoided.

5. *Dynamic analysis of tissue regions* For each sample measurement, a sample configuration is set-up to define the region mask files from GeoPIXE from step 2, the edge positions of the H OA-STIM signal and also if void region suppression is to be performed. By convention in LINAEUS, region-0 corresponds to the entire field of view and region-1 is a void area outside of the tissue covered region. The final step is the Dynamic Analysis. This creates image maps of the major elements and calculates the C, H , N and O edge heights and major element composition for each region. The elemental image data for each region is output in grey scale .png (loss-less) format. The elemental composition and edge heights for the major elements for each region are output in .csv files. This data is then subsequently manually input into the lesser- and trace element X-ray yield calculations in GeoPIXE.

6. *Calculation of lesser- and trace element compositions in GeoPIXE* The final step is to input for each region, the corresponding matrix composition and thickness from LINAEUS into the GeoPIXE X-ray yield calculation. Since the matrix compositions and thickness may change from one tissue region to another, it is necessary to re-fit in GeoPIXE the prototype spectrum and re-sort the data for each region in the sample.

   Then the molarity x_i (moles dm^{-3}) of lesser-/trace-element i for each tissue region is,

$$x_i = 10^{-3} \left(\frac{m_i}{m_m} \right) \frac{m_m}{A_i} \frac{1}{T}. \quad (1)$$

   The term in parenthesis is the dry mass ratio (μg/g) from GeoPIXE, m_m (g) the mass of the matrix and T (cm) the thickness of the the frozen ex vivo tissue section. A_i is the atomic mass of element i expressed in u. The factor 10^{-3} is included because the dry mass ratio is in units of μg/g and the molarity is defined as moles per dm^3. m_m in terms of the regional atomic concentration a_j (cm^{-3}) of H, C, N and O and their atomic masses A_j is.

$$m_m = \sum_{j=C,H,N,O} a_j A_j = \rho t, \quad (2)$$

   here, t is the thickness (cm) and ρ the density (g cm^{-3}) of the dry mass tissue. A subtle point in equations 1 and 2 is that because the tissue thickness from OA-STIM is the thickness of the tissue covered area, x_i is the molarity of the tissue without voids. This molarity calculation using equations 1 and 2 and the associated uncertainty calculations are trivial and conveniently carried out using a standard spreadsheet program based on the composition and thickness and their uncertainties from LINAEUS

3 Experimental

To illustrate the use of the LINAEUS code suite, a section of murine intestine was analysed. The subject was a cull animal that was maintained under a holding permit from the University of Louisiana at Lafayette Animal Care and Use Committee. Isoflurane (C_3OF_5Cl) inhalation followed by cervical dislocation was used for euthanasia. This recommended method[21] was not expected to significantly influence the elemental composition of tissue because isoflurane has a high vapour pressure (39 kPa at 25 °C) and any unbound residual will be lost during drying and exposure to the analysis vacuum. The data set and sample used here was part of another on-going study on the same subject. The small intestine was chosen because it is an organ with a pronounced structure with different tissue types[3,10,22,23]. The small intestine epithelium along with other mucosal tissues are the site of the immune system's primary layer of defence against infection. In this regard, trace elements such as Ca, Fe and Zn play an important role in immune system signalling. After euthanasia the small intestine was immediately dissected out and wiped clean using lint-free tissue. No washing with phosphate buffer solution or water was employed. The intestine sample was placed in an

View Article Online
DOI: 10.1039/D5JA00505A

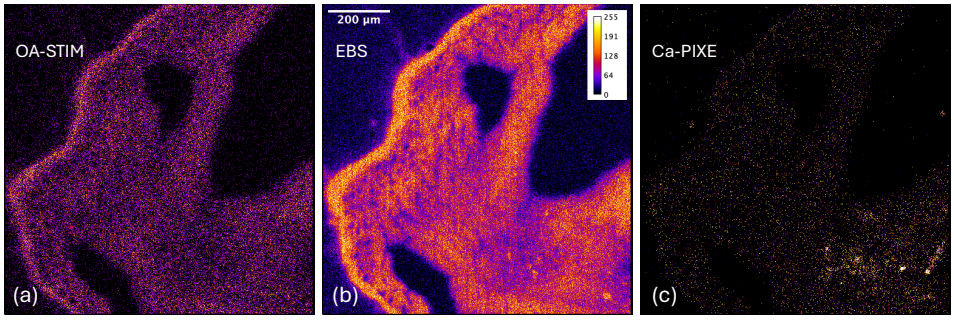

Fig. 4 Raw data images from GeoPIXE of mouse small intestine. (a) OA-STIM H, (b) EBS for all elements, (c) Ca Kα PIXE. The images have been contrast normalised to enhance visibility.

embedding mould and embedded in Optimum Cutting Temperature compound (OCT)[24] and cooled to -85 °C then stored on dry ice. Cryosectioning into stections of thickness $T = 15\mu$m was carried out at -16 °C using a Tanner Scientific TN50 rotary cryomicrotome[25]. Subsequently, the sections were transferred to supporting Pioloform films[19,26] on M8 stainless steel washers. The tissue section samples were allowed to dry overnight in a filtered air stream prior to shipping.

The EBS, OA-STIM and PIXE measurements were carried out using the MeV ion microprobe at the Tandem Laboratory, Uppsala University[27,28]. This uses a standard Oxford quadrupole triplet lens configuration with a standard Oxford microbeam analysis chamber. EBS measurements used an annular Au/Si surface barrier detector at a scattering angle of 170°. OA-STIM used a 3 mm × 3 mm Si p-i-n detector collimated to 2.5 mm at the scattering angle of 45°. The PIXE data was measured using a Princetown Gamma Tech (PGT) Si:Li detector with 30 mm^2 area nominal 3 mm thickness and 12.5 μm thick Be window and 50 12.5 μm Mylar filter. The experimental configuration is illustrated in Figure 3. A 2 MeV proton beam of 2 nA current, focused to a $\sim 3\,\mu$m $\times 3\,\mu$m beam spot was used. The beam-charge pulses (0.1 nC) were digitised and recorded along with the X- and Y- pixel coordinates, and the EBS-, OA-STIM- and PIXE-energy detector signals using a FastComTec-MPA-3 data acquisition system in event mode. The peaks corresponding to scattered H from H, C and O[19] from a pristine Pioloform film was used both for energy calibration and as a composition reference for these elements in OA-STIM and EBS. As noted above in Section 1, since no suitable N thin film standard material was available, the N concentration calibration was obtained by scaling from the oxygen calibration according to the differential scattering cross sections from refs[29–31]. Solid Au as well as a Cu grid and graphite sample were used to calibrate the energy of the EBS spectra. Pioloform was used to calibrate the OA-STIM spectra. The Mα 2.123 keV and Lγ_1 13.382 keV X-ray lines from the solid Au sample were also employed to calibrate the PIXE detector. These calibration points spanned the energy region of interest for PIXE analysis of lesser- and trace-life elements as well as the major elements measured with EBS and OA-STIM.

4 Results and Discussion

4.1 Selection of tissue-regions with GeoPIXE

Figure 4 presents the raw OA-STIM, EBS and Ca K PIXE images from GeoPIXE that were used to assign the regions of interest in the section of the intestine. The Ca PIXE map showed small regions with strongly enhanced Ca levels. The other lesser- and trace-element maps (P, S, Cl, K, Co, Mn, Fe, Co, Ni, Cu, Zn, etc.) were unremarkable. In interpreting these images it should be born in mind that the images represent a 2D section through an intestine sample which is convolved in 3D. Hence, the lumen region appeared collapsed and within the tissue. The different tissue-types (e.g. epithelium, submucosa, muscularis externa etc.) were nominally identified according to the tissue morphology of the tissue region[3,10,22,23].

Figure 5 presents the corresponding EBS and OA-STIM energy spectra. To obtain the H-image plot in Figure 4 (a) an energy window spanning the H signal in the OA-STIM spectrum was applied. Similarly, for Figure 4 (b) the EBS signals from the C, N and O peaks were selected while omitting the (lower energy) nuclear resonance peaks. (These appear between 700 and 950 keV in Figure 5(a).) Figure 6 presents the corresponding PIXE spectrum with the position of the X-ray lines for lesser- and trace life-elements marked. Figure 7 delineates the different tissue-regions selected for analysis. Region (0) was taken to be the entire image. Region (1) represents a void area used to identify the void areas as described above. Regions (2)-(4) and (10) correspond to different tissue-types with different morphology. The Ca regions (5)-(9) in Figure 7(b) correspond to small concentration "hot-spots" with strongly enhanced Ca levels compared to surrounding tissue observed in Figure 4 (c).

4.2 Non-linear fitting of the prototype EBS spectrum

Region 0, which covered the entire image field seen in Figure 7 was used to fit the prototype EBS spectrum shown in Figure 8. The fitting function (See Supplementary material †) is the sum of three trapezoid functions that represent the shape of the C, N and O contributions to the spectrum around the surface edge. The surface edges are convoluted with Gaussian functions that represents the EBS detector resolution function. The fitting of the surface edge heights over many channels yielded a more accurate determination of the surface edge heights because of the reduced counting statistical uncertainty. Fitting the four free pa-

View Article Online
DOI: 10.1039/D5JA00505A

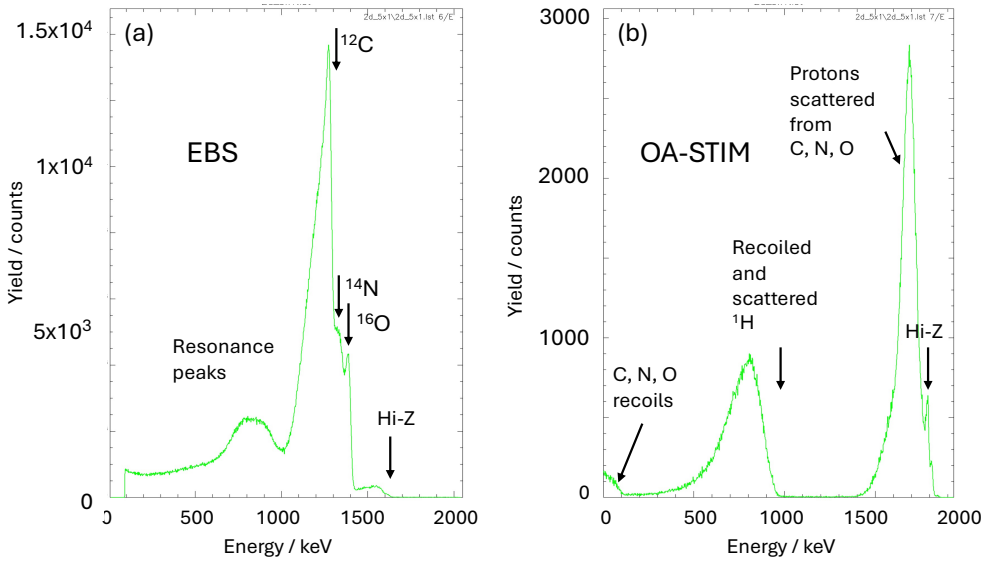

Fig. 5 Raw EBS and OA-STIM energy spectra from GeoPIXE for the data corresponding to Figure 4 (a) and (b).

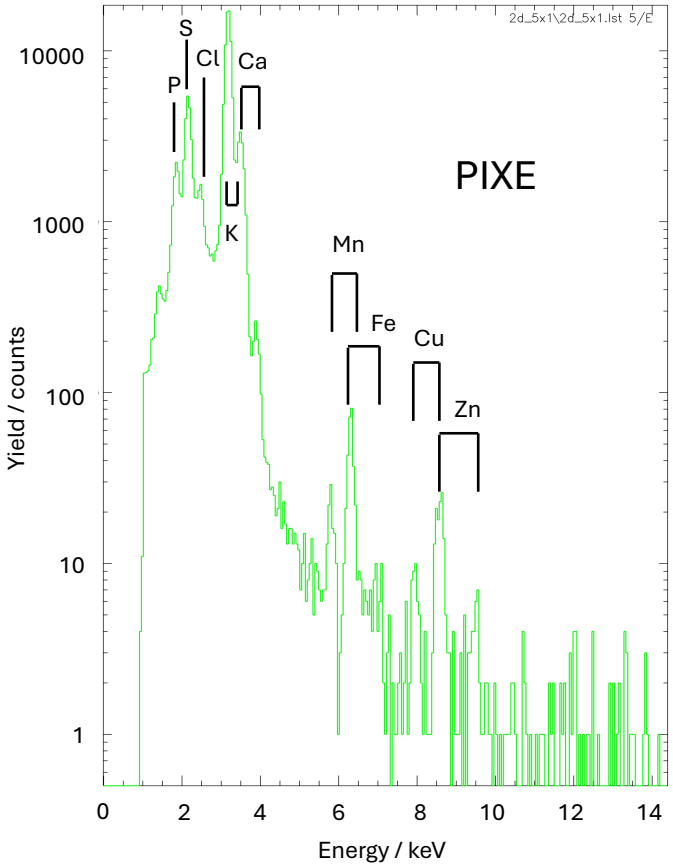

Fig. 6 Raw PIXE energy spectrum from GeoPIXE for the data corresponding to Figure 4 (c).

rameters for each of the C, N and O signals individually over selected ranges of channels limited undesirable divergence of the fit compared to simultaneous fitting of the C, N O with 12 free parameters over the entire fitting range. As a general precaution, the energy range of the fit was selected to avoid the resonances in the EBS spectra at ~ 1700 keV incident proton energy from ^{12}C, ^{14}N and ^{16}O[30–32]. The apparent negative slope for the N-signal compared to that for C and O could not be explained by the energy dependence of the energy loss[33] or scattering cross sections[30–32]. It may be a consequence of the significant contribution in region (0) from the significant area of voids where the C and O edge height is only contributed to by the Pioloform support film.

4.3 Dynamic Analysis of the major elements

Figure 9 shows the C, H, N and O elemental maps obtained from the Dynamic Analysis step without applying any void-region suppression. The tissue (light contrast) region in the N elemental map (Figure 9(c)) is well distinguished from the void regions where only the supporting (Pioloform) film is present. The H-image (Figure 9 (b)) does not show any significant signal in the void areas because the background H-signal associated with the Pioloform support film has been subtracted. On the other hand the C and O signals (Figure 9(a) and (d)) do exhibit signal in the void regions. This could be attributed to the sensitivity of EBS to the composition of the outer surface layer which in the void region corresponds to the C and O content of the Pioloform support film. The N image (Figure 9(c)) exhibits no signal in the void areas because Pioloform does not contain any N. The void-regions in the tissue correspond to features such as blood vessels, lymph canals, villi etc. (Figure 1) as well as regions outside of the tissue covered region. This implies that, *if not suppressed, the void-regions will introduce a systematic error in measured regional C, H, N and O compositions*. The importance of this can be judged from the fact that many tissue types contain large numbers of blood vessels, lymph canals, crypts and villi.

View Article Online
DOI: 10.1039/D5JA00505A

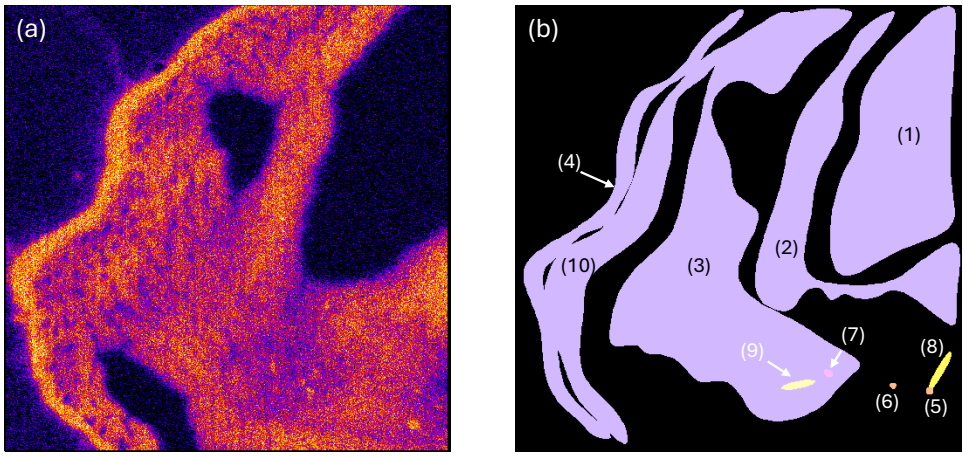

Fig. 7 Selected tissue-regions. (a) EBS map (b) Tissue-regions. Key: 1: void area, 2: Connective tissue, 3: Epithelium, 4: Muscularis externa, 10: submucosa, 5; Ca hot-spot-I, 6, Ca hot-spot-II, 7: Ca hot-spot-III in region 3, 8: Enhanced Ca, 9: Enhanced Ca in region 3.

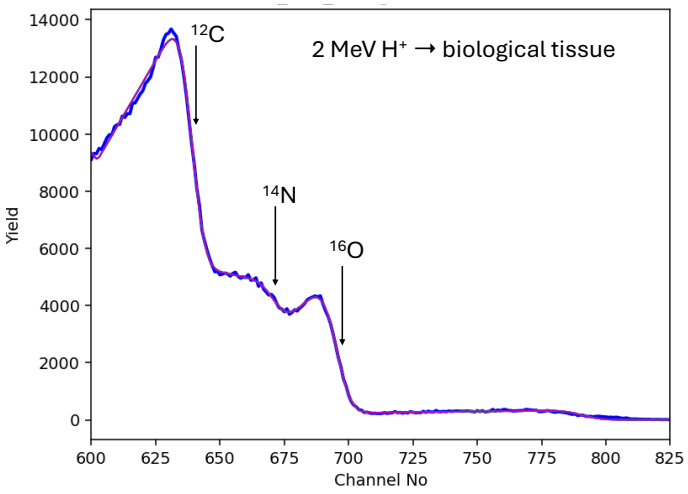

Fig. 8 Fitted prototype EBS spectrum from a biological tissue sample. The blue line denotes the experimental data and the red line the fitted spectrum function. The energies corresponding to the EBS surface edges are ^{12}C: 1432 keV, ^{14}N: 1502 keV and ^{16}O: 1557 keV.

4.4 Void-area suppression

The basis of the void suppression implemented in LINAEUS is to segment the H image on a pixel by pixel basis into tissue and void areas. The H-signal was used for computational efficiency since this is also used to correct the regional H-yield to compensate for the H contained in the supporting film. Moreover, the H-signal has less graininess than the N signal, which can only originate from tissue, giving better tissue–void discrimination.) Figure 9 revealed that the tissue- and void-areas could be visually differentiated based on the degree of graininess. The segmentation procedure is implemented in LINAEUS which is based on a comparison of the spatial frequency associated with the graininess in the H-image compared to that from a well-defined void area[20]. This is done by convolution of the element image with a filter with a circular kernel. The radius of the filter kernel was taken to be the mean radius between non-zero H-pixels in the void area[20]. The resulting spatially-filtered image was then bi-level segmented into tissue and void pixels by the algorithm thresholding the filtered image at the 50th percentile. The LINAEUS segmentation procedure is objective and does not involve any free parameters. The detailed mathematical basis of this algorithm is described elsewhere[20]. Using this algorithm, the H, C, N and O surface-edge heights and hence atomic composition from the EBS and OA-STIM signals could be objectively differentiated at the pixel level from that originating from the Piolofiorm support film.

Figure 10 presents the segmented image of Figure 9 (b). Comparison of these figures reveals that the two segments are well-distinguished from each other.

The void-suppression dilates the void-areas because the algorithm rejects some tissue pixels, particularity in thin regions at the selvedge of the void areas. The void-suppression dilates the void-areas because the algorithm rejects some tissue pixels, particularity in thin regions at the selvedge of the void areas. This has the advantage that only the tissue well away from voids contribute to the major element composition and thickness determination. However, this can also be a potential drawback because it may suppresses the small contributions from thin tissue areas where different cell types may be present. This may be assessed by comparing the map of the area assigned to tissue produced by LINAEUS e.g Fig 7 of ref.[20]. Where, the composition of thin selvedge tissue around the void regions is needed e.g. for the muscularis external (Region 4, Figure 7 (b)). This may be measured by manually assigning a region enclosing selvedge tissue and analysing this with void suppression turned off. The void dilation effect can be minimised by using images with good counting statistics and using thin supporting films or membranes that do not contain hydrogen (e.g. Si, Si_3N_4, although the later can introduce other challenges.

View Article Online
DOI: 10.1039/D5JA00505A

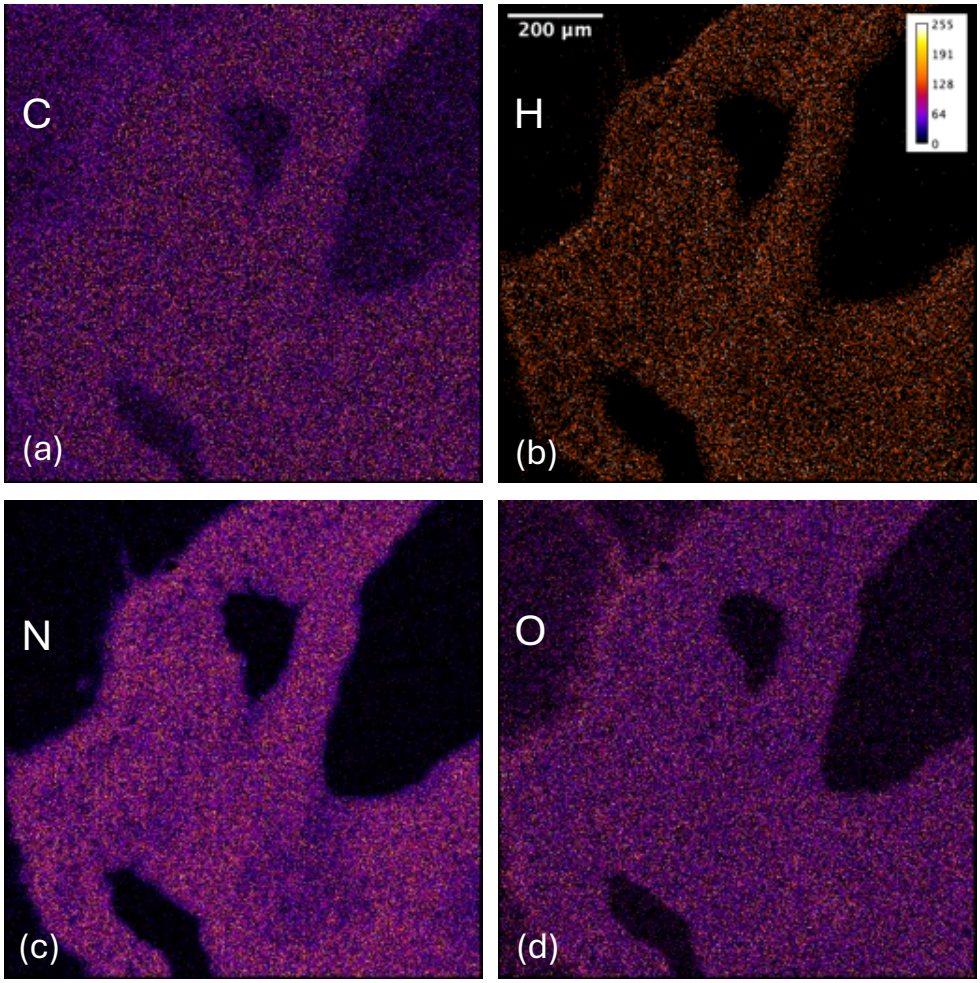

Fig. 9 Major element maps for (a) C, (b) H, (c) N and (d) O from Dynamic Analysis. The image contrast has been modified to improve visibility. No void-region suppression has been employed.

View Article Online
DOI: 10.1039/D5JA00505A

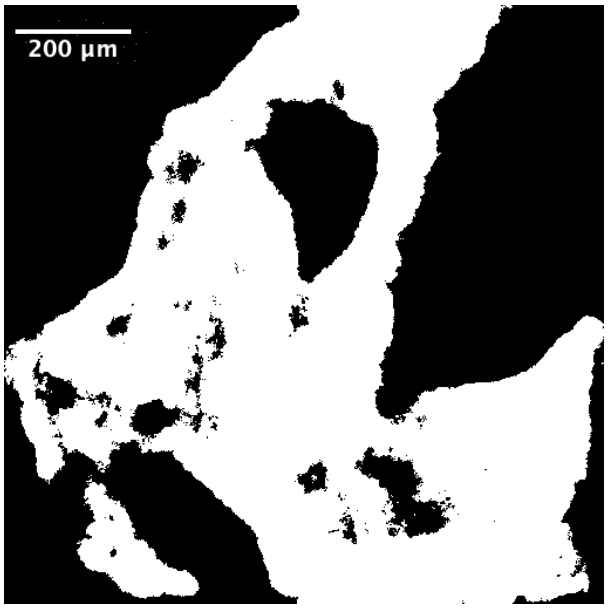

Fig. 10 Void- and tissue-region segmentation of the data in Figure 9. The white contrast represents tissue areas assigned as tissue.

4.5 Regional Matrix C, H, N, O contents and thickness

The major elemental maps in the tissue sample (Figure 11) exhibited a uniform contrast over the entire tissue-section region. This indicates there are no strong differences in major element contents for the different tissue-types present.

The atomic fractions for C, H, N for the different tissue regions are presented in Figure 12. The concentrations of H, C and O differed from each other with H making up about 50 at.% of the atomic composition fraction which is typical for many organic matrices. Consistent with exhibition of a lack of contrast between major elements (Figure 11) the regional compositions of H, C and O did not exhibit any statistically significant differences. A weak enhancement of N-content was however seen in the connective muscularis externa tissue. This could possibly be associated with a misassignment of connective tissue as muscle tissue. Here, the criteria for statistical significance was taken to be two standard deviations (viz. overlapping error bars in Figure 12). The distribution of the C, H, N and O contents was similar for all tissue-types in the ranges; H 50–53 at.%, C 20–23 at.%, N 8.8–12.4 at.%, and O 18.6–24 at.%. The mean overall composition for all regions was $C_{0.212\pm0.035}H_{0.486\pm0.088}N_{0.096\pm0.019}O_{0.206\pm0.031}$ which is in agreement with our previous data for porcine intestine [10].

The measured regional thicknesses are presented in Figure 13. Unlike the atomic compositions, the thickness differences between tissue-regions are statistically significant with variations of a factor ~ 2.5. Mechanical distortion of the measured tissue sections such as curling resulting from dehydration, could lead to a change in measured thickness that would influence the X-ray yields, but would not influence the tissue composition. The density used to determine the thickness in μm units (1.3 g cm^{-3}) was taken to be constant and that of dehydrated rat intestine [34]. This density value cancels out in the molarity calculation and was only included to allow easy import of matrix data to GeoPIXE.

4.6 Lesser- and trace-element contents

The measured regional major element compositions (Figure 12) and thickness (Figure 13) from LINAEUS were used as input data for the GeoPIXE X-ray yield calculation for each tissue-region. In GeoPIXE fresh X-ray yield calculations, non-linear fits and resorting of event mode file was performed for each tissue region. Figure 14 presents the lesser and trace element contents in terms of dry mass ratios (μg/g) for each region from GeoPIXE. The error bars in this figure correspond to one standard deviation of the statistical counting uncertainty σ. Taking the Method Detection Limit (MDL), for PIXE determination of the presence of an element a the sample to be the minimum detection level, to be 2σ, implied that P, S, Cl, K, Ca and Fe are detected in all tissue regions of the sample and Mn was detectable with $\sim$99 % confidence in the connective tissue and epithelium. Zn was also detected in all tissue regions except for the submucosa. This lesser- and trace-element content is typical for dry tissue sections of animal tissues [1,3,9,10].

Using the matrix element contents and thickness from LINAEUS and the dry mass ratios for the lesser- and trace-elements from GeoPIXE in equations 1 and 2 the molarities were determined. The resulting lesser and trace-element molarities are presented in Figure 15. The P, S and K concentrations are significantly higher than Cl and the trace elements Ca, Fe and Zn. The Fe concentration is significantly higher in the submucosa and might be associated with transport of haemoglobin in this tissue which is rich in blood vessels. Although OCT can penetrate and fill large void regions, it is unlikely to penetrate small capillaries and lymph canals resulting in trapping of Fe in this tissue region.

Comparing figures 13 and 14, it was observed that the elemental concentrations were not correlated in the different tissue regions. The molarities exhibit less variation between tissue regions than the dry tissue section mass ratios. This could be attributed to the different tissue section thickness as illustrated in Figure 13. This confirms that determination of the atomic composition of the dry tissue section matrix and thickness is critical to determine the trace element molarity of tissue sections using PIXE.

In common with our previous studies, [3,5,9,35] small regions $\lesssim 30\,\mu$m size with enhanced Ca concentration were observed in the epithelial tissue (Figure 4 (c)). The composition and thickness of these Ca "hot-spots" did not present adequate statistics in the C, H, N, O matrix element signals so the matrix composition and thickness of the surrounding epithelial tissue was used in Equation 2. Figure 16 shows an estimate of the Ca molarity in these hot-spots was enhanced by up to 50 times compared to the epithelial tissue. It was noted that the K signal was weakly enhanced in the hot spots. This is most likely an artefact from superposition of the tail of the very strong Ca Kα peak in these regions into the background tail signal in the K Kα and Kβ energy spectrum. The origin of these Ca hot-spots remains unclear. Ca is an important signal substance and Ca that is dynamically changing between being in state of incorporation in mineralisations,

View Article Online
DOI: 10.1039/D5JA00505A

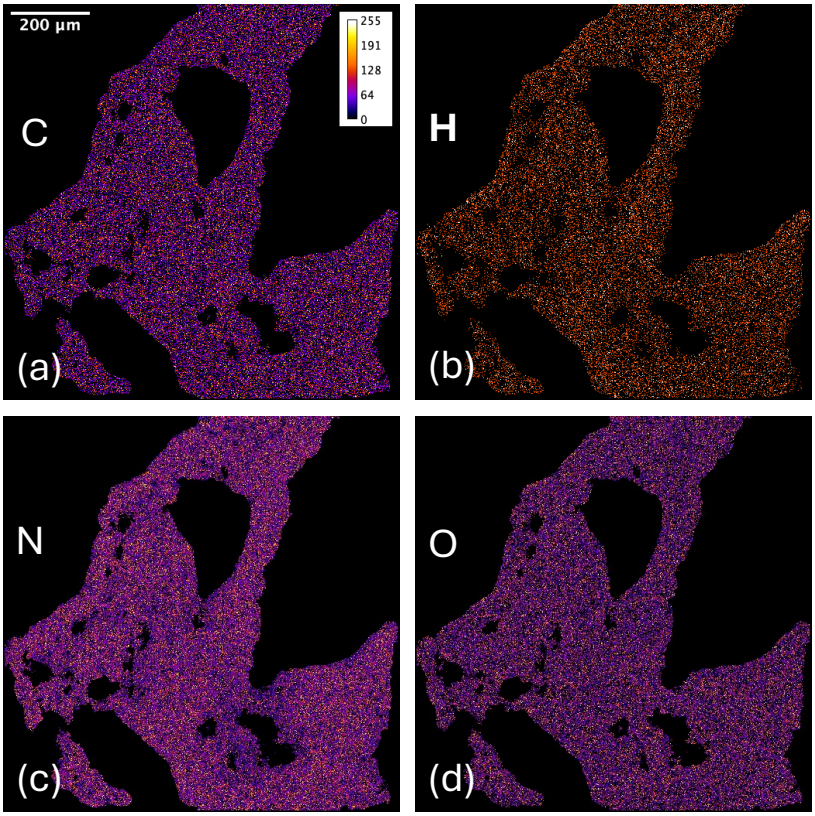

Fig. 11 Major element maps for (a) C, (b) H, (c) N and (d) O for the data in Figure 9 after void suppression using the mask in Figure 10 (c). The image contrast has been normalised to improve visibility.

View Article Online
DOI: 10.1039/D5JA00505A

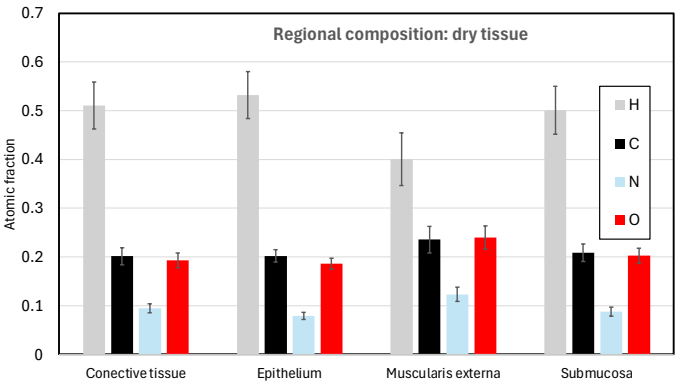

Fig. 12 Regional atomic fraction for major elements in the dry tissue section. The error bars represent one standard deviation.

bound to proteins and as Ca^{2+} ions.

$$Ca_{mineral} \rightleftharpoons Ca^{2+} \rightleftharpoons Ca_{bound} \quad (3)$$

The Ca hot-spot concentrations in Figure 16 are very high which could be characteristic of mineral particles. In biological systems Ca mineralisation is commonly in the form of calcite $CaCO_3$ (e.g. avian and reptilian eggshells[36]) or calcium hydroxyapatite $Ca_{10}(PO_4)_6(OH)_2$ which is the mineral content of bone and teeth. If mineralisation was present, corresponding C or P hot-spots should be observed in the elemental maps for C (Figure 9(a) and P (data not shown). Inspection of the elemental maps revealed no evidence of corresponding C and P hot-spots, suggesting the Ca-hotspots are instead associated with protein-bound Ca. Since the Ca hot-spots were located in the intestinal epithelium these may have been ingested with food. (We have previously reported Pb hot-spots in an archive sample of simian jejunum that were likely caused by the animal ingesting lead-based paint[3].) Ca hot-spots have also been observed in the nasal mucosa epithelium and mesenteric lymph node of virus-infected subjects[5,9]. Ingestion sources for the Ca hot-spots are possible for the nasal and intestinal mucosa but unlikely in the lymph node.

Our data was compared with some literature reference values[37,38] intended for radiation hygiene and radiology applications where the major element contents play a more important role. The agreement (Figure 17) is poor. However, the provenance of the standard tabulated values are generally unspecified and often only given to one significant digit.

5 Uncertainty contributions

The acceptable level of measurement uncertainty for a particular application of the LINAEUS code suite depends on the goal of the particular study. Generally, stochastic effects govern the uncertainty when relative measurements are made. When absolute comparisons with different measurements or tabulated values (viz. Figure 17), systematic contributions to uncertainties need also need to be considered. There are three quantities of interest when LINAEUS and GeoPIXE are used together to determine lesser- and trace-element molarities in dry and ex-vivo tissue samples. (i) The C, H, N, O atomic composition of the dry tissue section. (ii) The thickness t of the dry tissue section. (iii) The molarity of the lesser- and trace elements x_i. (i)–(iii) are interrelated and this makes exact determination of the uncertainties in the final result inherently non-trivial.

To facilitate handling of uncertainties, Table 1 presents the stochastic and systematic uncertainty sources that contribute to the uncertainties in the measured quantities, (i) - (iii). The uncertainties coverage was taken to be $\pm 2\sigma$ where σ is the standard deviation. The uncertainty sources in Table 1 are considered to be uncorrelated and geometrically summed. Some uncertainty sources that cancel out, or have small residuals were omitted from Table 1. An example is the dry tissue matrix density which is input data to GeoPIXE but provided the sample is thin from a PIXE analysis viewpoint (See Supplementary material †) cancels-out to first order in the molarity determination (equations 1 and 2).

The analysis goes over the computational steps; composition $\longrightarrow$ dry-tissue thickness $\longrightarrow$ molarity. Consideration of covariational uncertainty contributions showed that the energy shift of the H-signal in the OA-STIM spectra and the stopping cross sections entered into the composition and thickness calculations. The contribution to the uncertainty in thickness was small and dominated by the uncorrelated contribution from H-peak area counting statistics. Stopping uncertainties contributions are small as these contributions are largely canceled out in the composition detemination they enter as propotinally in the thickness and thence the molarity determinations.

Table 1 Stochastic and systematic uncertainty sources in LINAEUS

Source	Stochastic	Systematic	Refs.
Dry tissue: atomic composition			
Counting statistics	11%		
Stopping		0.5 %	39,40
Braggs rule deviation		≤0.01%	41
$(d\sigma/d\Omega_N)/(d\sigma/d\Omega_O)$		4%	29–31
Reference composition		1.8%	19
Sums	11%	4.8%	
	Total	**12%**	
Dry tissue: thickness			
Energy loss	3.3%		
Atomic composition (above)		0.7%	
Stopping cross Section		2 %	39,40
Braggs rule deviation		≤0.04%	41
Energy calibrations		0.6 %	
Void area suppression	2 %		
Sums	3.9%	3.0%	
	Total	**4.9%**	
Ex vivo tissue: molarity			
GeoPIXE counting statistics	10 %		
Ionisation cross section		5%	42
X-ray fluorescence yield		4%	43
Microtome section thickness		3.3 %	
X-ray filter thickness		0.06 %	
Ion charge collection		0.1 %	
Sums	10 %	6.8 %	
	Total	**12.1%**	

5.1 Stochastic contributions

Generally, when different tissue regions in the same sample, or comparison between different samples in the same measurement sequence are compared, only contributions to the relative uncertainties are important. Inspection of Table 1 shows that a domi-

View Article Online
DOI: 10.1039/D5JA00505A

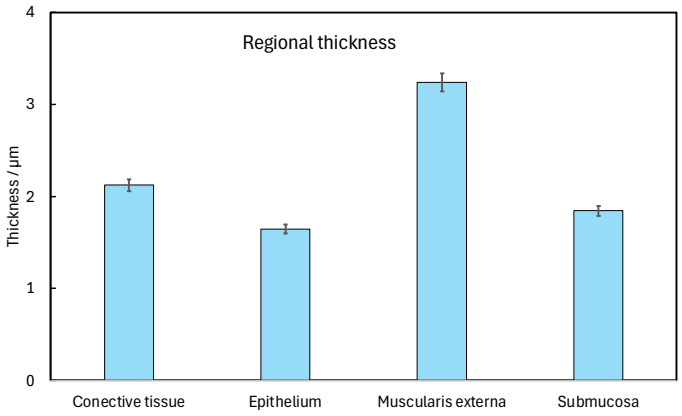

Fig. 13 Regional thickness for different tissue regions. The error bars represent the error in determining the dominating uncertainty in determining the H surface edge position (± 3 %.

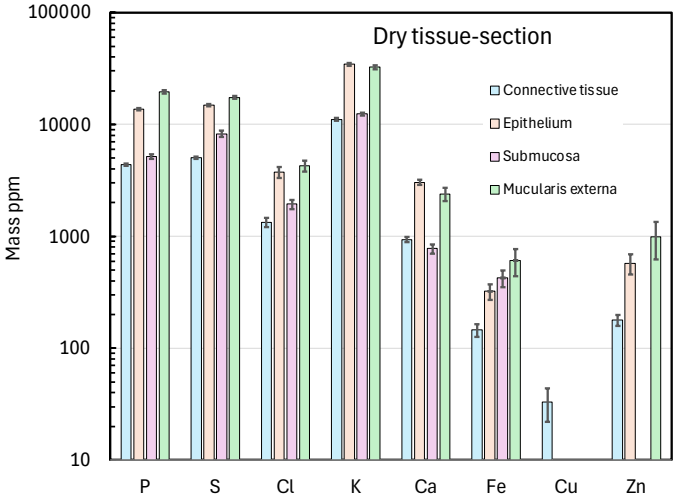

Fig. 14 Trace and minor element concentrations in the dry tissue section for the connective tissue, epithelial, submucosa and muscularis externa tissue regions. The error bars correspond to one standard deviation (See text).

nating stochastic contribution to the three measured parameters arises from counting statistical variations. This is calculated in LINAEUS from the fitting of the edge-heights and the counts under the H-peak in the OA-STIM and the C and O peaks in the EBS spectra, respectively, for the reference material. The stochastic uncertainty in the surface-edge heights is calculated in LINAEUS from the edge height fitting parameter curvature in parameter space.

5.2 C, H, N and O dry tissue composition uncertainties

As noted previously, a thin-film ($\leq 1\mu$m) C–H–O reference standard is used in LINAEUS to avoid the systematic uncertainties associated with the scattering cross sections for H[8], C[29,32] and O[29,31]. This introduces additional stochastic uncertainties from the counting statistical variations in the C, H and O signals from the reference sample. These stochastic contributions cancel out in relative measurements but contribute to absolute measurements. Pioloform[19] was employed as a thin-film reference standard. Even if Pioloform is a random terpolymer, the atomic composition is only weakly dependent on the polyvinyl achohol (PVA) content[19]. The calibration factor for N was in this case determined from the ratio of EBS scattering cross sections from SigmaCalc[29] for $(d\sigma/d\Omega)_N/(d\sigma/d\Omega)_O$.

The ion stopping enters via the ratio of the stopping cross section factors for the different major elements (Supplementary material †). Here DPASS stopping[33,39,40] is used because in OA-STIM the stopping cross section factor is related to the difference in stopping on the inward an outward paths[8]. In connection with this deviations from Bragg's rule may contribute a few % deviation in the stopping for protons traversing light C–H–N–O containing materials[41]. This largely cancels-out in the determination of the atomic composition for the dry tissue film.

The effect of dehydration induced morphological changes can increase the local thickness. This is apparent from local changes in the dry tissue thickness without and change in the elemental composition. The corresponding changes in the lesser-and trace-element molarities are compensated out by the change in local thickness.

5.3 Dry tissue thickness determination

The main stochastic contribution originates from the determination of the H-surface edge energy position and counting statistics. This is also contributed to by the small systematic uncertainty to the shift in edge energy from the OA-STIM calibration. This contribution mostly comes from the uncertainty in determining the H half-height position in the OA-STIM spectrum due to the effects of film thickness variations[8]. It will vary from one tissue region to another and will affect relative comparisons for different tissue types. Unlike the case for the dry tissue atomic composition determination, the effects of stopping such as the effect of departures from Bragg's rule are uncompensated. It is noted in this connection that, unlike the EBS case, the OA-STIM stopping cross section factor (Supplementary material †) is the difference between two stopping cross sections at different proton energies[8,9]. For this reason, the DPASS stopping[33] which is based on ab-inito approach[39,40] is preferable on self-consistency grounds because unlike quasi-empirical predictor coded (viz. SRIM[44,45]) it is uninfluenced by uncertainties in individual experimental stopping data sets. The atomic composition uncertainty also contributes a systematic uncertainty to the tissue thickness determination.

View Article Online
DOI: 10.1039/D5JA00505A

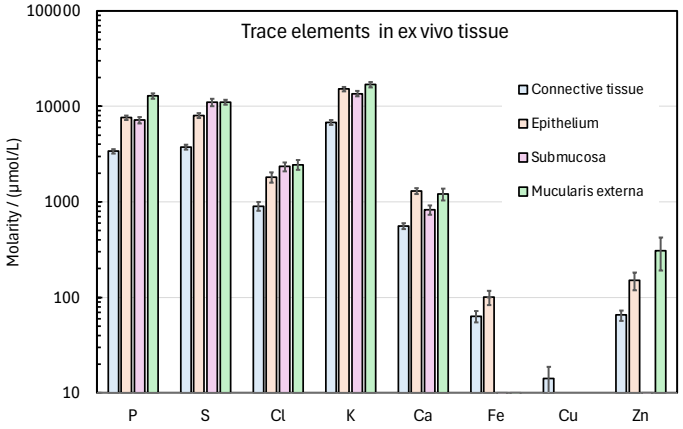

Fig. 15 Ex vivo trace and minor element molarities for the connective tissue, epithelial, submucosa and muscularis externa tissue regions. The error bars correspond to one standard deviation (See text). Elemental molarities less than the MDL of the PIXE measurement are omitted.

5.4 Uncertainties in lesser and trace element determination

The uncertainty in the molarity of lesser and trace elements is significantly contributed to by the contributions from the measured lesser-/trace-element content N_i from GeoPIXE (Table 1). Additional contributions originate through equations 1 and 2 to the uncertainties in the dry tissue atomic composition and dry tissue thickness discussed above and the charge collection used to determine the beam flux.

Considering first the PIXE lesser-/trace-element uncertainty contributions. The stochastic uncertainty in the trace element molarity is related to the counting statistical effects on the dry mass ratio m_i/m_m This stochastic uncertainty is calculated by GeoPIXE from the curvature of the fitting matrix[11].

If the sample approximates to a thin sample so that the integrals in the full X-ray yield equation (Supplementary material †) become unity and can be neglected, then the characteristic X-ray yield becomes,

$$Y_i = N_i N_0 \frac{\omega_\nu \sigma_i b_\nu t_f(E_\nu)\,\varepsilon(E_\nu)\,\Omega_{det}}{4\pi}. \quad (4)$$

With, N_i the number of i lesser-/trace-element atoms per unit area N_0 is the number of ions, Ω_{det} the solid angle subtended by the detector. The quantities that depend on the characteristic X-ray line with energy E_ν are: σ_i the ionisation cross section, ω_ν the fluorescence yield, b_x the branching fraction, $t_f(E_\nu)$ the transmission of the filter for X-rays with energy E_ν and ε_{E_ν} the detector efficiency. Unless special care is taken, ω_ν has an uncertainty of ± 7 %. For Si detectors with thickness $> 300\mu$m the $\varepsilon(E_\nu)$ is $\simeq 100$ % and is energy independent over the range 2 - 10 keV which corresponds to K X-rays from most life elements. The transmission through the X-ray filter $t_f(E_\nu)$ is more problematic as discussed below.

Dominating systematic contributions to the uncertainty in the PIXE measurement originate from the statistical cross section for characteristic X-ray production. This is the product of the ionisation cross section, the branching ratio and the fluorescence yield. The branching ratio is set by quantum mechanics according the line widths corrrsponding to the sub-shells[7]. The uncertainty in the absolute ionisation cross section[42] and fluorescence yield[43] used in GeoPIXE have uncertainties of ± 5 %. Another important contribution comes from the thickness of the X-ray filter foil which can introduce a significant systematic uncertainty because of the exponential dependence of the attenuation on the filter thickness. For a 50 μm Mylar film with $\pm 0.4\,\mu$m thickness deviation (used here) the systematic uncertainty for heavy trace elements Ca – Zn the contribution is small ($\leq\sim 0.6$ %). However, as the atomic number decreases the attenuation and systematic uncertainty increases reaching ~ 1.4 % for P Kα. The final contribution to the uncertainty in the lesser-/trace-element molarity comes from the number of incident ions which is determined from the electrical charge deposited in a Faraday cup by the ions that pass through the sample. The main uncertainty contribution to this parameter originates from secondary electrons that escape from the Faraday cup, which based on solid angles is 0.06 %. The uncertainty in the electrical calibration was estimated to be 0.05 %.

The uncertainty in the section cut with the cryomicrotome also contributes a systematic uncertainty. This to some degree depends on the skill of the operator. Areas with severe folding and piling up (Figure 1) can be identified in the OA-STIM image as having a contrast corresponding to thicker layers. Most rotary cryomicrotomes advance the knife-edge perpendicular the rocking sample by means of a lead-screw translation mechanism. Precision lead-screw devices such as linear translation devices typically achieve a setting accuracy of $\pm$ 0.3 μm for small translations such as those corresponding to the 12 μm sections used here (e.g. ref.[46], Figure 1 of ref.[47]).

The void-suppression algorithm considerably reduces the systematic uncertainty associated with the void areas influencing the molarity measurements. However, this uncertainty is not completely suppressed because any thin selvedge areas around the voids which do not satisfy the tissue segment criteria will be treated as void area. These thin regions may be made up of cells with a different type and hence composition that will contribute to the PIXE signals, but not the thickness and major element composition of the tissue. Although the effect will cancel out in the lesser- and trace-element molarity determinations, it will influence the major element composition and thickness of the dry tissue segment. An estimated level of 3 % selvedge around a region gives a < 3 % major element composition and thickness error since the selvedge is thin and then will contain a smaller fraction of lesser and trace elements.

5.4.1 Approaches to control uncertainties

Some consideration should be given to control the uncertainty contributions. For example, by careful selection of the image regions for analysis to minimise inclusion of voids the small uncertainty introduced by the void-suppression algorithm can be minimised. Another example is the use of a N-containing reference composition sample. The use of a N-containing reference standard will reduce the systematic uncertainty in the dry tissue film composition. Unfortunately, few suitable thin-film standard materials exist although possibly this issue could be mitigated by using multiple reference standards.

View Article Online
DOI: 10.1039/D5JA00505A

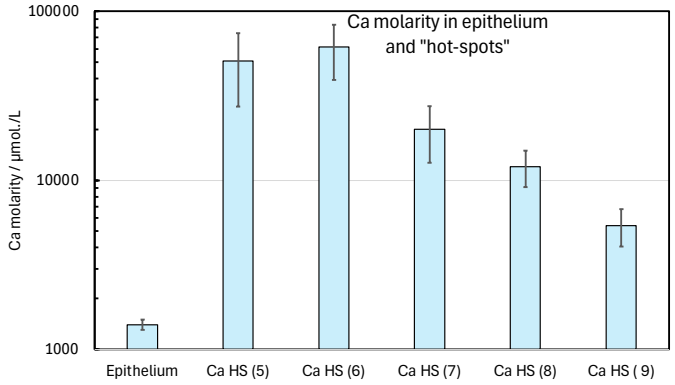

Fig. 16 Ex vivo Ca molarities in small "hot-spots" with enhanced Ca (Ca HS) and surrounding epithelial tissue. The numbers in parentheses denote the regions shown in Figure 7. The error bars correspond to one standard deviation (See text). Elemental molarities less than the MDL of the PIXE measurement are omitted.

The largest uncertainty in the lesser- and trace-element molarity determination is associated with the X-ray ionisation cross sections and fluorescence yields. These together with the contributions from the X-ray filter thickness, detector efficiency and solid angle could be mitigated by using reference materials. The usual wet-chemical approach is to "spike" a homogeneous sample with known quantity of a reference substance. This cannot be used here because of the inherent natural inhomogeneity of the sample. Since the ionisation cross section and fluorescence yields varies from element to element an indirect method to calibrate each element of interest is needed. This approach would normalise out to a considerable extent the uncertainties associated with characteristic X-ray absorption and production.

The absolute uncertainties (Table 1) are at first sight poor in comparison with wet-chemical methods. However, wet chemical approaches need large sample volumes (mm^3) that preclude analysis of single tissue section. The present method can analyse extremely small regions ($\sim 1000 \mu m^2$) within small volumes (typically, 1 mm $\times$ 1 mm $\times$ 15 μm). This corresponds to a total sample mass of $\sim$1.5 ng. Microdissection in conjunction with wet-chemistry could be used to perform similar analysis. However, this is tedious and the need to use samples from multiple subjects would preclude study of one-of-a-kind subjects. A further advantage over microdissection is that the high sensitivity allows tissue sections cut adjacent to the one used for microprobe analysis to be used for conventional histological or immunological staining to reveal other spatially relevant features.

6 Conclusions

1. The LINAEUS software code suite has been implemented to facilitate determination of the major element (H, C, N and O) contents and thickness of tissue sections.

2. The matrix composition and thickness data is used together with micro-PIXE analysis using the GeoPIXE code to determine the molarities of lesser- and trace-element in ex vivo tissue samples.

3. A void suppression algorithm, together with subtraction of the H-signal from the supporting film mitigates systematic uncertainties in the major C, H, N, O composition associated with void regions from blood vessels, lymph canals etc.

4. The use of the code has been demonstrated to measure Ca, Fe and Zn in mouse small intestine. Small highly localised regions containing Ca were observed in the intestine tissue.

5. The main contribution to composition uncertainties originates from stochastic counting uncertainties from the reference and sample measurements.

6. The main uncertainty in the absolute value of the lesser- and trace-element molarities originates from the ionisation cross sections and X-ray fluorescence yields and can be mitigated using standards.

Author contributions

Harry J. Whitlow: Conceptualization, Methodology, Software, Validation, Writing- Original draft preparation, Supervision, Investigation, Project administration **Gyula Nagy:** Investigation, Visualization, Writing - Review and Editing **Robert J.W. Frost:** Investigation, Writing - Review and Editing **Donruedee Toyen:** Investigation, Validation, Writing - Review and Editing **Deepanwita Bose:** Investigation, Writing - Review and Editing **Aaron McLaughlin:** Investigation **Karen M. Smith:** Writing - Review and Editing **Chris G. Ryan:** Conceptualization, Methodology, Software, Writing - Review and Editing **Andrej Kuznetsov:** Investigation, Supervision, Writing - Review and Editing **Alexander Azarov:** Investigation, Writing - Review and Editing **Francois Villinger:** Project administration, Supervision, Writing - Review and Editing

Conflicts of interest

There are no conflicts to declare.

Animal ethics statement

All animal procedures were performed in accordance with the Regulations from the Institute for Laboratory Animal Research Guide to the Care and Use of Laboratory animals, and the principles outlined in guidance of the Association for Assessment and Accreditation of Laboratory Animals Care, Inc. The breeding, maintenance and use of the animals were reviewed and approved by the University of Louisiana at Lafayette Institutional Animal Care and Use Committee.

Additional material

The datasets generated during and/or analysed during the current study are not publicly available due to large raw-data filesizes but are available from the authors on reasonable request. Technical details of the LINAEUS code suite are provided in the Supplementary material †. The current LINAEUS code suite version in an "as-is" state is available from the principle author without any warranty.The GeoPIXE code is available as Open Source software[48].

View Article Online
DOI: 10.1039/D5JA00505A

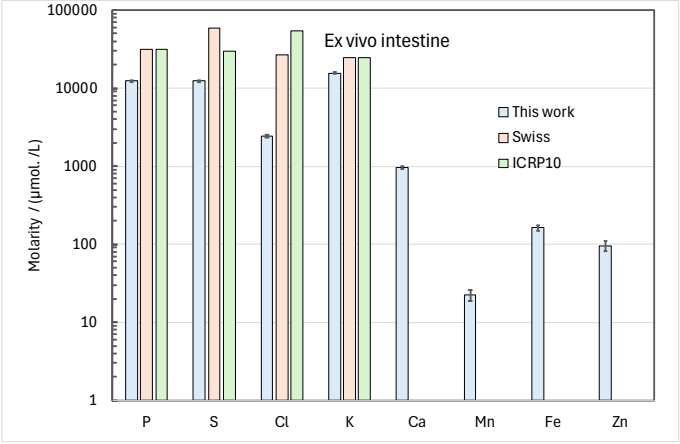

Fig. 17 Comparison of mean lesser- and trace-element molarity in ex vivo tissue with literature data.

Acknowledgements

The concept for non-linear fitting of EBS data was due to the late Eric Læsgård, Aarhus University, Denmark.

The project was supported by the The Office of the Vice President for Research, Innovation, and Economic Development of the University of Louisiana at Lafayette. Accelerator operation in Uppsala was supported by the Swedish Research Council VR-RFI (Contract No. 2019-00191). HJW acknowledges support from The Research Council of Norway for the Norwegian Micro and Nano-Fabrication Facility, NorFab (Project 11 No. 245963.) HJW's research is partially supported by Magnus Bergwalls Stiftelse (2024-1327). DT is supported by a Thailand Royal Golden Jubilee Fellowship (N41A650069)

Notes and references

1 H. J. Whitlow and M.-Q. Ren, in *Ion Beam Analysis: fundamentals and applications*, ed. M. Nastasi, J. W. Mayer and Y. Wang, CRC Press, Talor & Francis Group, Boca Raton FL, 33487, USA, 2015, ch. 14 Biomedical Applications, pp. 309–337.

2 M.-Q. Ren, Y.-T. Zhou, H.-X. Chen, T.-Y. Li, S. K. Vajandar, T. Osipowicz, F. Watt and C.-W. Li, *Allergy*, 2018, **73**, 724–727.

3 H. J. Whitlow, N. T. Deoli, A. de Vera, K. Morgan and F. Villinger, *physica status solidi (a)*, 2021, **218**, 2000107.

4 Bureau International des Poids et Measures, *The International System of Units (SI)*, 2019.

5 H. J. Whitlow, G. Nagy, N. Henderson, R. Greco, N. Deoli, K. M. Smith, K. Morgan and F. Villinger, *Nuclear Instruments and Methods in Physics Research Section B: Beam Interactions with Materials and Atoms*, 2023, **539**, 152–161.

6 E. N. Marieb, *Human Anatomy & Physiology*, Pearson Benjamin Cummings, 6th edn, 2004.

7 *Ion Beam Analysis: fundamentals and applications*, ed. M. Nastasi, J. W. Mayer and Y. Wang, CRC Press, Talor & Francis Group, Boca Raton FL, 33487, USA, 2015.

8 H. J. Whitlow, *Nuclear Instruments and Methods in Physics Research Section B: Beam Interactions with Materials and Atoms*, 2023, **540**, 51–61.

9 H. J. Whitlow, A. Kuznetsov, A. Azarov, G. Nagy, R. J. Frost, N. Henderson, R. Greco, N. Deoli, K. M. Smith, W. Sudprasert, S. Amphalop, W. Insuan, S. Wichianchot, M.-Q. Ren, T. Osipowicz, C. G. Ryan and F. Villinger, *Nuclear Instruments and Methods in Physics Research Section B: Beam Interactions with Materials and Atoms*, 2024, **554**, 165411.

10 H. J. Whitlow, G. Nagy, A. Kuznetsov, R. J. Frost, A. Azarov, K. M. Smith, S. Amphalop, W. Insuan, S. Wichianchot, M.-Q. Ren, T. Osipowicz, C. G. Ryan, W. Sudprasert and F. Villinger, *physica status solidi (a)*, 2025, **222**, 2400161.

11 C. Ryan, D. Cousens, S. Sie, W. Griffin, G. Suter and E. Clayton, *Nuclear Instruments and Methods in Physics Research Section B: Beam Interactions with Materials and Atoms*, 1990, **47**, 55–71.

12 C. Ryan, *Nucl. Instrum. and Meth. B*, 2001, **181**, 170–179.

13 C. Ryan, D. Jamieson, C. Churms and J. Pilcher, *Nucl. Instrum. Meth. B*, 1995, **104**, 157–165.

14 C. Ryan and D. Jamieson, *Nuclear Instruments and Methods in Physics Research Section B: Beam Interactions with Materials and Atoms*, 1993, **77**, 203–214.

15 C. G. Ryan, *International Journal of Imaging Systems and Technology*, 2000, **11**, 219–230.

16 R. Norarat, H. J. Whitlow, M. Ren, T. Osipowicz, J. A. van Kan, J. Timonen and F. Watt, *Microelectronic Engineering*, 2013, **102**, 6–8.

17 A. Gurbich, *SigmaCalc*, 2015, `http://sigmacalc.iate.obninsk.ru`.

18 A. Gurbich, *Nuclear Instruments and Methods in Physics Research Section B: Beam Interactions with Materials and Atoms*, 2016, **371**, 27–32.

19 H. J. Whitlow and G. Nagy, *Nuclear Instruments and Methods in Physics Research Section B: Beam Interactions with Materials and Atoms*, 2023, **539**, 136–140.

20 H. J. Whitlow, R. Norarat, R. J. Frost, A. Ghosh, D. Toyen, D. Bose, A. McLaughlin and F. Villinger, *Ultramicroscopy*, 2026, **281**, 114299.

21 S. Leary and et al., *AVMA Guidelines for the Euthanasia of Animals: AVMA Guidelines for the Euthanasia of Animals: 2020 Edition*, American Veterinary Medical Association technical report.

22 K. Delbaere, I. Roegiers, A. Bron, C. Durif, T. Van de Wiele, S. Blanquet-Diot and L. Marinelli, *FEMS Microbiology Reviews*, 2023, **47**, fuad022.

23 E. N. Marieb, *Human Anatomy & Physiology*, Pearson Benjamin Cummings, 6th edn, 2004, pp. 907–910.

24 Sakura Finetek USA Inc., 1750 West 214th St. Torrance, CA 90501, USA, *Safety Data sheet Tissue-Tek® O.C.T. Compound*, 2016.

25 *Tanner scientific TN50 and TN50UV cryostats*, "Mercedes Scientific, 12210 Rangeland Parkway, Lakewood Ranch FL 34211, USA".

View Article Online
DOI: 10.1039/D5JA00505A

26 M.-Q. Ren, *PhD thesis*, Faculty of Mathematics and Natural Sciences, University of Jyväskylä, Finland, 2007.

27 G. Nagy, H. J. Whitlow and D. Primetzhofer, *Niclear Instruments and Methds: Section B*, 2022.

28 D. Papaioannou, G. Nagy, D. Primetzhofer and R. J. W. Frost, *The European Physical Journal Plus*, 2025, **140**, 585.

29 A. Gurbich, *Nuclear Instruments and Methods in Physics Research Section B: Beam Interactions with Materials and Atoms*, 2016, **371**, 27–32.

30 A. Gurbich, *Nuclear Instruments and Methods in Physics Research Section B: Beam Interactions with Materials and Atoms*, 2008, **266**, 1193–1197.

31 A. Gurbich, *Nuclear Instruments and Methods in Physics Research Section B: Beam Interactions with Materials and Atoms*, 1997, **129**, 311–316.

32 A. Gurbich, *Nuclear Instruments and Methods in Physics Research Section B: Beam Interactions with Materials and Atoms*, 1998, **136-138**, 60–65.

33 P. Sigmund and A. Schinner, *DPASS*, 2020, `https://www.sdu.dk/en/dpass`.

34 R. F. Reinoso, B. A. Telfer and M. Rowland, *Journal of Pharmacological and Toxicological Methods*, 1997, **38**, 87–92.

35 H. J. Whitlow, N. Henderson, R. Greco, N. Deoli, K. M. Smith, K. Morgan and F. Villinger, *Journal of Physics: Conference Series*, 2022, **2326**, 012010.

36 N. T. Deoli, A. Mikolajczyk, Z. Fusilier, M. Zappi and H. J. Whitlow, *Nuclear Instruments and Methods in Physics Research Section B: Beam Interactions with Materials and Atoms*, 2021, **502**, 80–84.

37 I. Foundation, *Tissue properties: Database: Elemental composition*, `https://itis.swiss/virtual-population/tissue-properties/database/elements/`.

38 H.G.Menzel, C. Clement and P. DeLuca, *Ann ICRP*, 2009, **32**, 1–164.

39 P. Sigmund and A. Schinner, *Nuclear Instruments and Methods in Physics Research Section B: Beam Interactions with Materials and Atoms*, 2002, **195**, 64–90.

40 A. Schinner and P. Sigmund, *Nuclear Instruments and Methods in Physics Research Section B: Beam Interactions with Materials and Atoms*, 2019, **460**, 19–26.

41 D. I. Thwaites, *Nuclear Instruments and Methods in Physics Research Section B: Beam Interactions with Materials and Atoms*, 1992, **69**, 53–63.

42 D. Cohen and M. Harrigan, *Atomic Data and Nuclear Data Tables*, 1985, **33**, 255–343.

43 M. O. Krause, 1979, **8**, 307–327.

44 J. Ziegler, *Interactions of ions with matter*, website, 2013, `"www.srim.org"`.

45 J. F. Ziegler, J. P. Biersack and M. D. Ziegler, *SRIM, the Stopping and Range of Ions in Matter*, SRIM Company, 2008.

46 M. Newport, *Motorized Linear Stage, Miniature, 25 mm Travel, DC Motor, M2 and M3*, `https://www.newport.com/p/MFA-CC)`.

47 H. Whitlow, S. Gorelick, N. Puttaraksa, M. Napari, M. Hokkanen and R. Norarat, *Nuclear Instruments and Methods in Physics Research Section B: Beam Interactions with Materials and Atoms*, 2013, **306**, 307–310.

48 *GeoPIXE*, GitHub, `https://github.com/CSIRO-GeoscienceAnalytics/GeoPIXE`.

View Article Online
DOI: 10.1039/D5JA00505A

The datasets generated during and/or analysed during the current study are large raw-data files and are available from the authors on reasonable request. Technical details of the LINAEUS code suite are provided in the Supplementary material. The current LINAEUS code suite version in an "as-is" state is available from the principle author without any warranty. The GeoPIXE code is available as Open Source software on GitHub.